Fluidized bed hydrodynamic modeling of CO_2 in syngas: Distorted RTD curves due to adsorption on FCC

Ariane Bérard[a], Bruno Blais[a], Gregory S. Patience[a]

[a]*Department of Chemical Engineering, Polytechnique Montréal, C.P. 6079, Succ. CV Montréal, H3C 3A7, Québec, Canada*

Abstract

The hydrodynamics of gas-phase fluidized beds is non-ideal due to high velocity. Micro-fluidized beds have distinct flow patterns because of the wall and the diameter constrains bubble velocity. We measured the gas phase RTD in a 8 mm ID quartz tube loaded with fluid catalytic cracking catalyst (FCC). We devised a feed manifold to introduce a 4-component tracer gas as a bolus pulse. The FCC separated the gases based on diffusivity like chromatography. At ambient temperature, the trailing edge of CO, CH_4, and CO_2 have extended tails and an axial dispersion model accounts only for 92 % of the variance. We developed a model to characterize the tailing that includes diffusion from the bulk gas to the FCC pores and adsorption-desorption of the gas on the catalyst. This model accounted for 98.6 % of the variance in the RTD. At 300 °C the tailing disappeared consistent with expectations in chromatography.

Keywords: residence time distribution, mathematical modeling, adsorption, diffusion, hydrodynamic

1. INTRODUCTION

Residence time distribution (RTD) is a fundamental technique applied mainly in mixing, reactor science, biomass and pharmaco-kinetics[1, 2, 3, 4, 5]. This method consists of injecting a tracer in a vessel and to measure its concentration with time. Researchers apply RTD for gas [6], solids [7] and liquids

[8]. RTD test is more commonly an experimental procedure but researchers are also applying as a post-processing tool for computational fluid dynamics (CFD) results[9, 10, 11]. Both methods detect back-mixing, dead volume, channeling, and dispersion by comparing against the ideal plug flow model.

RTD of the gas phase in fluidized bed reactors [12] is particularly interesting as the hydrodynamics in these systems comprise several phenomena—bubble phase, emulsion phase, grid regions, and the transport disengagement section above the bed. Indeed, as a function of the tracers injected and the catalyst loaded, RTD analysis differentiates between diffusion, dispersion, and adsorption[1]. To describe these phenomena, researchers have developed several models — the one, two or three phases model, the axial dispersion model, the tanks-in-series, and regression model[13, 14].

The one phase model or homogeneous bed model considers exclusively the emulsion phase. This is the case of the axial dispersion model, predominately applied for RTD with the Peclet number ($N_{\mathrm{Pe}} = uZ/\mathcal{D}$) as the prime fitted parameter where $\mathcal{D}$ is the axial dispersion coefficient. The nondimensional form is [15, 10, 16]:

$$\frac{\partial C}{\partial \theta} + \frac{\partial C}{\partial \xi} = \frac{1}{N_{\mathrm{Pe}}} \frac{\partial^2 C}{\partial \xi^2} \tag{1}$$

where C is the concentration, θ is nondimensional time ($\theta = tu/Z$) and ξ is the nondimensional length ($\xi = z/Z$).

To characterize the complex phenomena in fluidized bed, researchers introduce the notions of bubbles, and the mass transfer between bubbles and emulsion—the two phases model. Also, they consider the cloud created by the movement of gas around each bubble [17]. The first approach of the model includes the cloud around the bubble with the emulsion phase [18]. In this case,

the mass transfer is between the bubble and the emulsion phase[19]:

$$\frac{dN_{\mathrm{A}}}{dt} = u_{\mathrm{b}} V_{\mathrm{bubble}} \left(\frac{dC_{\mathrm{A,b}}}{dz} \right) = K_{\mathrm{GB}} V_{\mathrm{bubble}} (C_{\mathrm{A}}^{i} - C_{\mathrm{A,b}}) \tag{2}$$

Where N_{A} is the mol of A, u_{b} is the bubble rise velocity, V_{bubble} is the volume occupied by the bubble phase, K_{GB} is the interchange coefficient between bubble and emulsion-cloud, C_{A}^{i} is the concentration of A at gas-particle interface, and $C_{\mathrm{A,b}}$ is the concentration of A in the bubble.

The second approach merges the cloud and the bubble into a single phase and the second phase is the emulsion. The mass transfer balance is [20]:

$$\frac{\mathrm{d}N_A}{\mathrm{d}t} = V_{\mathrm{cloud}} \left(\frac{\mathrm{d}C_{\mathrm{A,c}}}{\mathrm{d}t} \right) = K_{\mathrm{GC}} V_{\mathrm{cloud}} (C_{\mathrm{A,e}} - C_{\mathrm{A,c}}) = k_{\mathrm{GC}} S_{\mathrm{ex,cloud}} (C_{\mathrm{A,e}} - C_{\mathrm{A,c}}) \tag{3}$$

where, the index c represents cloud and e represents emulsion, V_{cloud} is the volume occupied by cloud and bubble, K_{GC} is the interchange coefficient between bubble-cloud and emulsion, k_{GC} is the mass transfer coefficient between bubble-cloud and emulsion, and $S_{\mathrm{ex,cloud}}$ is the exterior surface of clouds.

Finally, to approximate reality more closely, the 3-phase model introduces powder physico-chemical properties—porosity, and mass transfer from the gas in the emulsion to the particle surface. First, the flux equation for each phase is [21]:

$$w_{\mathrm{p}} = U_{\mathrm{g,p}} C_{\mathrm{p}} - M_{\mathrm{m,p}} \frac{\partial C_{\mathrm{p}}}{\partial x} \tag{4}$$

where w is the mass flux, C is the mass concentration, U_{g} is the gas velocity, and M is the axial mixing coefficient. The index p represents the phases: emulsion (E), bubble (B), or solid (S).

Additionally, the continuity equation for each phase is [21]:

$$\frac{\partial w_{\mathrm{p}}}{\partial x} + \frac{\partial C_{\mathrm{p}}}{\partial t} = r_{\mathrm{p}} \tag{5}$$

where r is the reaction rate. To solve equations 4 and 5 for three phases (E,B, and S), we suppose that the velocity and mixing coefficient of the solid phase is negligible ($u_{\mathrm{S}} = M_{\mathrm{S}} \approx 0$) [21].

The models proposed in the literature for RTD analysis in fluidized bed reactors have limitations:

1. Lack of the gas mass transfer mechanism between the pores inside the catalyst and its surface.
2. In general, reaction concepts are missing. Consequently, when adsorption occurs between the tracer and catalyst. The results diverge from the axial dispersion model.
3. Normally only single tracers are modeled. They may or may not characterize the system correctly (Ar and Kr radioactive gas tracers are excellent tracers but are poor models for hydrogen or methane). Each gas tracer is modeled independently. The injection of several tracers demonstrates how the hydrodynamics depend on the gas diffusivity (but this is most evident at ambient temperature).

In this article, we analyze the effect of porosity, and Geldart group A and B powders on RTD by injecting a syngas gas composition simultaneously (CO_2, H_2, CO, and CH_4) at ambient temperature and 300 °C. The phenomenon of diffusion and adsorption are the core of RTD analyzes. Then, we develop a new model to account for adsorption of gases on the catalyst since the RTD curve obtained experimentally deviates substantially from idealized flow patterns.

2. Experimental

2.1. Powders

We compared Fluid Catalytic Cracking Catalyst (FCC) from Total© with sand. They have distinct physico-chemical properties. FCC is a porous Geldart group A powder while sand is non-porous and belongs to the Geldart group B.[22] SEM images demonstrate the spherical shape of FCC and the angular shap of the sand (Figure 1). We confirmed the sphericity by applying the Ergun equation ($\phi_{\mathrm{FCC}} = 0.99$ and $\phi_{\mathrm{sand}} = 0.68$) :

$$\frac{\Delta P}{\Delta Z} = \frac{U_{\mathrm{g}}}{\phi d_{\mathrm{p}}} \frac{1-\epsilon_{\mathrm{v}}}{\epsilon_{\mathrm{v}}^3} \left(150(1-\epsilon_{\mathrm{v}}) \frac{\mu}{\phi d_{\mathrm{p}}} + 1.75 \rho_{\mathrm{g}} U_{\mathrm{g}} \right) \tag{6}$$

Where ΔP is the pressure drop, ΔZ is the bed height, ϵ_{v} is the void fraction, and μ is the viscosity.

The minimum fluidized velocity (U_{mf}), the bulk density (ρ_b) and the mean particle diameter (d_{50}) are 6, 1.6 and 1.4 times higher respectively for sand compared to FCC (Table 1). Inversely, the surface area (S_{A}) measured by BET is 166 times higher for FCC vs sand. However, the Hausner ratio (H_{r}) is similar for both powders. Thus, the hydrodynamic behavior diverges between the two powders since their physical characteristics are different.

2.2. Gases

To discern all phenomena (dispersion, diffusion and adsorption), RTD experiments are performed with syngas tracers. The bottle purchased from Air Liquide© contains 15 % CO_2, 15.3 % CO, 19.9 % H_2, 14.7 % CH_4, and the balance N_2. In all studies, the inert gas injected continuously is argon. These gases have a wide range of diffusivity at 25 °C and 300 °C (Table 2).

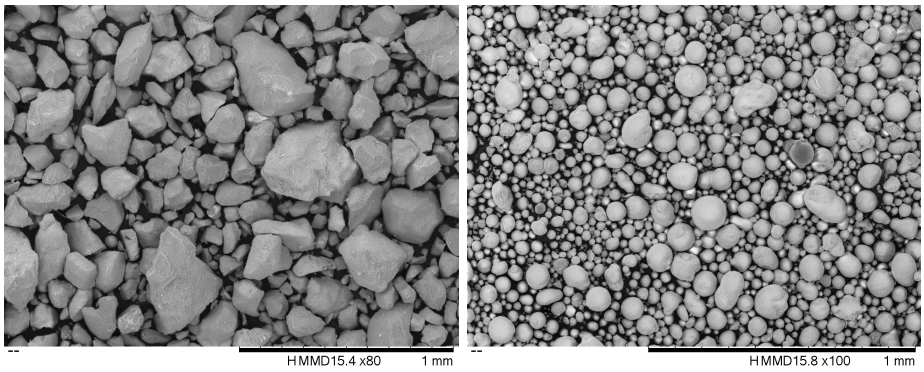

(a) (b)

Figure 1: SEM images of the powders: (a) Sand, large cuboid or polygonal particles; (b) FCC, most particles are spheroids.

2.3. Micro reactor set-up

The experiments were run at ambient temperature in an 8 mm diameter quartz tube 360 mm long (Figure 2). We poured 8.19 g of FCC or 13.5 g of sand to reach, for both, 180 mm tapped bed heights. For all experiments, two Brooks mass flow controllers (MFC) maintained the velocity at $10\,\mathrm{mm\,s^{-1}}$ which represents a Reynolds number (N_{Re}) of 6.8. We installed a Hiden quadrupole mass spectrometer (MS) with a pulse ion counting (SCEM) detector at the exit of the reactor to monitor the tracer concentration *on-line* [26]. The capillary is 0.90 m long, 0.20 mm internal diameter and it is heated at 160 °C. A vacuum pump maintained pressure at 6.2×10^{-5} mPa. A manifold with an 8-way valve and two identical sample loops make up the injection system [1]. Because the the same MFC injects the tracer into the reactor and the lines are identical with the same number of ports on the 8-way valve, the pressure drop across the two lines are identical and we expect only an imperceptible change in pressure when we turn the valve.

The sequence starts with the injection continuously of the inert— argon. Before reaching the reactor, argon passes through the first 10 mL loop. At the

Property	**FCC**	**Sand**	n	**Comments**
Composition	mixed[1]	Silica (SiO_2)	-	-
Geldart Group	A	B	-	-
U_{mf}, $mm\,s^{-1}$	2.2	13	1	-
ρ_b, $kg\,m^{-3}$	874(4)	1328(10)	5	Scott density
	853(19)	1366(27)	5	Poured density
	965(10)	1529(47)	5	Tapped density
	945	1426	1	Hg porosimetry
ρ_p, $kg\,m^{-3}$	1610	2279	1	Hg porosimetry
ρ_{sk}, $kg\,m^{-3}$	2360(2)	2777(5)	10	Gas
ϵ_v	0.44	0.37	1	-
H_r	1.13(3)	1.12(4)	5	Hausner ratio
θ_{angle}, °	24(1)	44(2)	6	Angle of repose
d_{10}, µm	39.4(4)	58(2)	3	Laser diffraction
d_{50}, µm	64.0(6)	87(2)	3	Laser diffraction
d_{90}, µm	104(1)	120(2)	3	Laser diffraction
ϕ	0.99	0.68	1	Ergun equation
S_A, $m^2\,g^{-1}$	93.28	0.56	1	BET
	34.52	0.41	1	BJH[2]
v_{pore}, $mL\,g^{-1}$	0.145	0.003	1	BJH[2]
d_{pore}, nm	38	21	1	BJH[2]

[1] FCC catalysts include a variety of zeolite crystallite sizes and particle properties [24]

[2] BJH: desorption branch

Table 1: FCC and sand properties [23]. The uncertainties represent standard deviation.

Gases	$\mathscr{D}$ $[cm^2\,s^{-1}]$ $T = 25°C$	$\mathscr{D}$ $[cm^2\,s^{-1}]$ $T = 300°C$	molar mass $[g\,mol^{-1}]$
CO_2	0.150	0.479	44
CO	0.195	0.622	28
CH_4	0.208	0.664	16
H_2	0.796	2.54	2

Table 2: Diffusivities in argon and atomic mass for gases. All diffusivities are calculated with the correlation of Fuller – Schettler – Gidding [25]. This method is available for non-polar gases at 101.25 kPa.

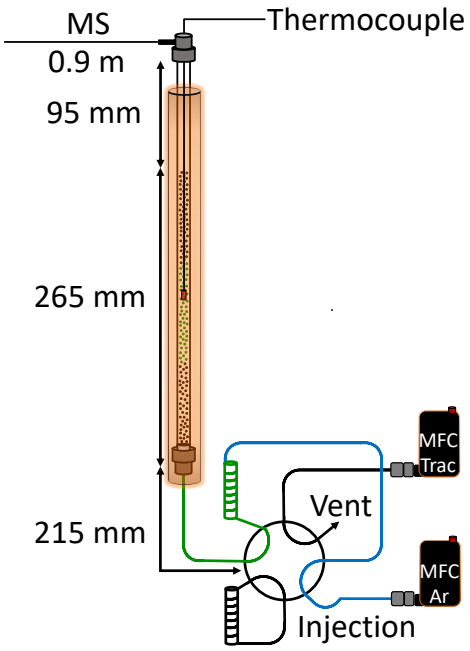

Figure 2: Fluidized bed reactor configuration surrounded by a furnace. The quartz tube was 8 mm diameter and 360 mm at 25 °C and or 320 mm at 300 °C. At room temperature, the tapped bed height with all catalyst was 180 mm and it expanded to an average of 265 mm when fluidized. At 300 °C, the tapped bed height is 130 mm. The mass spectrometer (MS) capillary is 0.9 mm long with a 0.20 mm internal diameter. First, the 8-way valve is in the filling position (not shown) where argon goes to the reactor and the tracer fills a 10 mL sample loop. Then, at time $t = 180$ s, we switch the 8-way valve to the injection position. Argon (blue line) sweeps the tracer (green line) from the loop to the reactor.

same time, the second 10 mL loop fills with tracer (and evacuates to exhaust). After a three minutes purge, we switched the 8-way valve. This corresponds to $t = 0$. The argon stream purges the second sample loop with the syngas tracer and enters the reactor. The stream entering the reactor is always controlled with the same MFC. The MS measured the concentration of all gases simultaneously at 2 Hz for 4 minutes after which we shut off the MS and purge the system with argon for 3 minutes before the beginning another experiment.

For experiments at 300 °C, the reactor is shorter— 32 cm and housed in an electrically heated furnace. The tapped bed height is 13 cm, so 6.50 g of FCC. We only tested FCC to study the effect adsorption at high temperature.

All plastic pipes around the reactor were changed for metal while we kept the same lengths and dimensions. We also added a thermocouple to measure the temperature in the catalytic bed. The experimental sequence wass exactly the same.

In accordance with Bérard et al. (2020) we minimized dead volume above and below the catalytic bed to ensure a maximize the contribution to the variance of the reactor[1]. For each set of experiments, we performed two RTD tests at the inlet of the reactor, and two at the outlet. For the axial dispersion model, we subtracted the RTD time at the inlet. For the new model, the entrance data are considered as the initial gas concentration.

2.4. Axial dispersion model

We fit experimental data with the the axial dispersion model (Equation 1). We applied the boundary conditions for a closed-open system [27, 16]:

$$C_{0,\xi} = 0, 0 \geq \xi \geq 1 \tag{7}$$

$$C_{\tau,0} = \rho_0, \tau > 0 \tag{8}$$

$$\frac{\mathrm{d}C_{\tau,1}}{\mathrm{d}\xi} = 0, \tau > 0 \tag{9}$$

The exact analytic solution is [16]:

$$G(\theta) = \frac{1}{2}\left[\mathrm{erfc}\sqrt{\frac{N_{\mathrm{Pe}}}{4\theta}\left(1-\theta\right)} + \mathrm{e}^{N_{\mathrm{Pe}}}\mathrm{erfc}\sqrt{\frac{N_{\mathrm{Pe}}}{4\theta}\left(1+\theta\right)}\right] \tag{10}$$

For each test, we normalized the data to reach the same area under the curve for each gas.

$$\mathrm{Area} = \frac{C_i}{\sum C_i \Delta t} \tag{11}$$

Then, we subtracted the initial time measured at the inlet of the reactor (MS capillary and inlet lines) to the total time at the exit. We minimized the sum of squares of the error (SSE) between the axial dispersion model and the experimental data to calculate N_{Pe}. Finally, to quantify the difference between the predictions and the data, we calculated the coefficient of determination (R^2).

The model adequately approximates pulse injections (no back-mixing) when we simulate each gas independently but the parameters for each gas are different. So, we developed a new model for multiple gases injection that accounts for the differences and the long tail (due to adsorption).

2.5. New Model-Mole balance equation

Reactor RTD analysis includes multiple phases and species particularly for porous solids and flow systems like fluidized beds. The literature often considers an emulsion phase, a bubble phase and at times a cloud phase and a wake. Since the bubble phase is assumed to have little catalyst, all reaction takes place in the emulsion phase (and cloud and wake). Here, we consider that bubbles form and disintegrate sufficiently rapidly that the gas phase is a continuum. Indeed, researchers achieve 100 % conversion in fluidized bed reactors which implies a rapid mixing between the bubble phase and the other phases. Consequently, this phase is neglected in the new model [28]. We consider catalyst as a distinct phase—solid phase. The third phase is the catalyst surface in its pores on which any species may adsorb. Thus, the new model considers three mole balances—the gas phase moving upwards, gas in the pores that follow the movement of the solids, and the adsorbed species on the catalyst surface (that also follow the solids motion). For the injection of multiple tracers, all gas species are dependent on each other. In fact, if species adsorb on the catalyst pores, this will have the consequence of reducing the total flow rate in the reactor. We included this dependence when we solved the model. The flow chart (Figure 3)

encompasses the principal steps of solving the model.

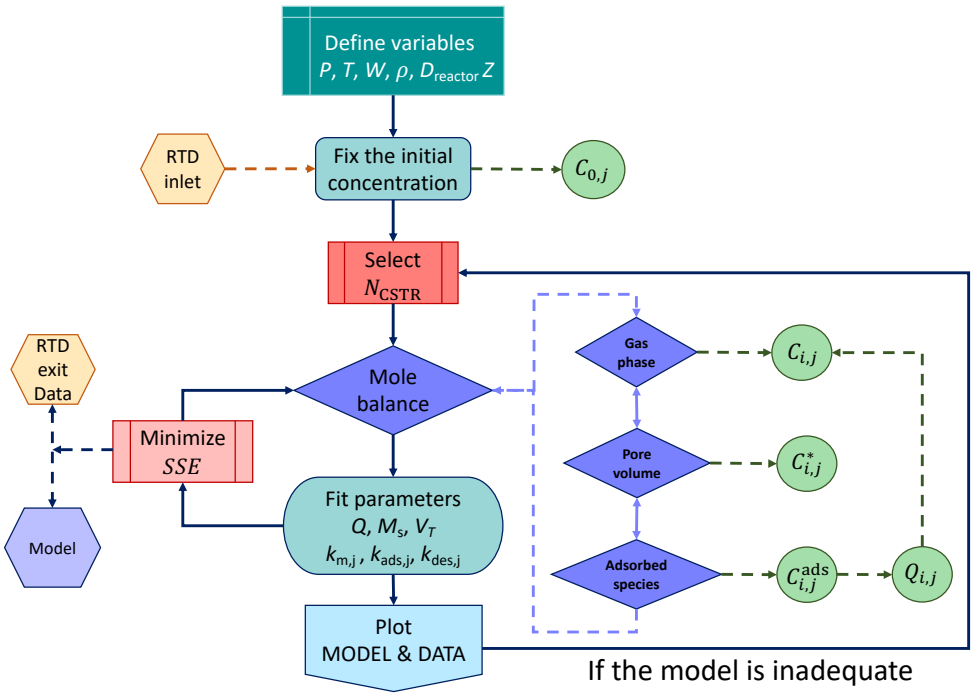

Figure 3: Flow chart of the resolution of the new model. Diamonds are equations to solve, hexagons are experimental data, and circles are the result variables for each species j. The model is inadequate if the model peak diverges from the experimental data or the R^2 is smaller compared to the axial dispersion model results. In this case, the number of CSTRs is modified.

2.5.1. Gas phase mole balance

In fluidized beds, when the gas velocity exceeds U_{mf} (minimum fluidization velocity), the pressure drop, ΔP is essentially constant and proportional to the bed density, $\rho_p(1-\epsilon_{\mathrm{v}})$, and the mass of catalyst in the reactor, W:

$$\Delta P = \rho_p(1-\epsilon)gZ = \frac{Wg}{X_{\mathrm{A}}} \tag{12}$$

So the molar density, $C_{i,j}$, varies with height, z, according to:

$$C_{i,j} = \frac{P_{i,j}}{RT} = \frac{P_{\mathrm{o}} - \frac{z_{i,j}}{Z}\Delta P}{RT} \tag{13}$$

Then, the mole fraction ($y_{i,j}$) for each specie is:

$$y_{i,j} = \frac{C_{i,j}}{\sum_j C_{i,j}} \tag{14}$$

As the bed expands, bubbles grow larger but frictional effects are minimal compared to the solids hold-up. Assuming that the pressure drop is negligible introduces an error of as much as 1 % with 10 g of catalyst in a reactor that has a diameter of 8 mm. For deep beds, we include the pressure variation with axial distance.

The volume of the gas phase (V_{g}) is $\epsilon_{\mathrm{v}}V$ while the volume of the gas in the particle phase (V_{p}) is $(1-\epsilon_{\mathrm{v}})\epsilon_{\mathrm{sk}}V$. The mass transfer coefficient—$k'_{\mathrm{m},j}$—accounts for molecular diffusion from the gas phase into the catalyst pores and r_j is the adsorption/desorption rate, which is proportional to the number of active sites, V_{A}. A convective term, Q_{rxn}, accounts for mass transfer between the two phases: when a species from the gas phase is in the pore, $C^*_{i,j}$, and adsorbs to a vacant site, V_{V}, on the catalyst surface creating an adsorbed species $C^{\mathrm{ads}}_{i,j}$. This reaction creates a convective flux, that acts like a vaccum. The flux from the bulk gas phase to the pore phase equal to the moles adsorbed. When the desorption rate becomes greater than the adsorption rate, the flux reverses and the convective flux is from the pore to the bulk gas phase. Every reaction, r_j, contributes to the molar flux between the phases at each grid block i, $\tilde{Q}_{\mathrm{rxn},i}$:

$$r^k_{i,j} = \left[k_{ads,j}C^{*,k-1}_{i,j}\left(V_{\mathrm{T}} - C^{\mathrm{ads,k-1}}_{i,j}\right) - k_{des,j}C^{\mathrm{ads,k-1}}_{i,j}\right]W_i V_{\mathrm{pore,i}} \tag{15}$$

$$\tilde{Q}_{\mathrm{rxn},i} = \sum_{j=1}^{N_j} r_{i,j}^{k} \tag{16}$$

where k_{ads} is the forward reaction—adsorption—and k_{des} is the reverse reaction—desorption.

The volumetric flow rate in the axial direction $Q_{i,j}^{k}$ is:

$$Q_{i,j}^{k} = Q_{i-1,j}^{k} + r_{i,j}^{k} \tag{17}$$

The axial volumetric flow rate at any height, Q_i, equals the inlet flow rate, Q_{o}, multiplied by the expansion due to the change in pressure plus the sum of the species that have adsorbed or desorbed to that point.

$$Q_i = Q_{\mathrm{o}} \frac{P_{\mathrm{o}}}{P_i} + Q_{i,j}^{k} \tag{18}$$

The differential form of the gas phase mole balance is:

$$\frac{\partial C}{\partial t} + U_{\mathrm{g}} \frac{\partial C}{\partial z} = \mathcal{D} \frac{\partial^2 C}{\partial z^2} + k_{\mathrm{m}}(C - C^*) + \frac{y_{i,j}^{k-1} \tilde{Q}_{\mathrm{rxn},i}}{V_{\mathrm{g}}} \tag{19}$$

With the finite volume approach form, when the adsorption rate is greater than the desorption rate ($k_{\mathrm{ads}} C_i^* V_{\mathrm{T}} > k_{\mathrm{des}} C_i^{\mathrm{ads}}$) the mole balance equation for species j in grid block i in the gas phase is:

$$\epsilon_{\mathrm{v}} V \frac{C_{i,j}^{k} - C_{i,j}^{k-1}}{\Delta t} = -Q_i^{k-1} \left(C_{i,j}^{k-1} - C_{i-1,j}^{k-1} \right)$$

$$-k'_{\mathrm{m,j}} \left(C_{i,j}^{k-1} - C_{i,j}^{*,k-1} \right) - y_{i,j}^{k} \tilde{Q}_{\mathrm{rxn},i} \tag{20}$$

where, $k'_{\mathrm{m,j}}$ is a fitting parameter. As gas species, j, adsorbs onto the catalyst surface the accompanying influx of gas from the bulk gas to the pore is the

product of the total moles reacted at that grid block multiplied by the mole faction of that species, $\tilde{Q}_{\mathrm{rxn},i}$.

When the adsorption rate is less than the desorption rate, the net flux is from the pore with a mole fraction y^* multiplied by the total moles of gas that evolve from the surface during that time step: ($k_{\mathrm{ads}} C_i^* V_{\mathrm{T}} < k_{\mathrm{des}} C_i^{\mathrm{ads}}$)

$$\epsilon_{\mathrm{v}} V \frac{C_{i,j}^{k} - C_{i-1,j}^{k-1}}{\Delta t} = -Q_i^{k-1} \left(C_{i,j}^{k-1} - C_{i-1,j}^{k-1} \right)$$

$$-k'_{\mathrm{m,j}} \left(C_{i,j}^{k-1} - C_{i,j}^{*,k-1} \right) + y_{i,j}^{*,k-1} \tilde{Q}_{\mathrm{rxn},i} \tag{21}$$

2.5.2. Pore volume mole balance

The hydrodynamics of the gas in the pore as well as the adsorbed species is dictated by the transport of the solids phase. The solids move up predominantly in the centre of the vessel and down along the the walls. This motion is well characterized for spouted beds, riser reactors, and larger sized fluidized beds. This movement ensures isothermal conditions and that the solids are perfectly backmixed. To represent it mathematically, we introduce a solids circulation term, M_{s}, (convective) in both the upward and downward directions and assume radial uniformity—perfectly backmixed). The mass flux, w_{s}, equals the quotient of the solids circulation rate and the cross-sectional area. The gas velocity (U_g) is:

$$U_{\mathrm{g}} = \frac{w_{\mathrm{s}}}{\rho_{\mathrm{p}}} = \frac{M_{\mathrm{s}}}{X_{\mathrm{A}} \rho_{\mathrm{p}}} \tag{22}$$

where ρ_{p} is the particle density. The bulk density and skeletal densities are:

$$\rho_{\mathrm{b}} = \rho_{\mathrm{p}}(1 - \epsilon_{\mathrm{v}}) \tag{23}$$

$$\rho_{\mathrm{sk}} = \frac{\rho_{\mathrm{p}}}{1 - \epsilon_{\mathrm{sk}}} \tag{24}$$

The convective contribution to the mole balance of the pore phase ($\tilde{Q}_{\mathrm{rxn},i}$) is analogous to that of the the gas phase mole balance. The differential form of the pore volume mole balance is:

$$\frac{\partial C^*}{\partial t} = \mathcal{D}_{\mathrm{S}} \frac{\partial^2 C^*}{\partial z^2} - k_{\mathrm{m}}(C - C^*) + W_{\mathrm{i}} \left[k_{\mathrm{ads}} C^* (C_{\mathrm{T}} - C^{\mathrm{ads}}) - k_{\mathrm{des}} C^{\mathrm{ads}} \right] \tag{25}$$

where $\mathcal{D}_{\mathrm{S}}$ is the dispersion coefficient for the solid phase.

When the adsorption rate is greater than the desorption rate ($k_{\mathrm{ads}} C^*_{i,j} V_{\mathrm{T}} > k_{\mathrm{des}} C^{\mathrm{ads}}_{i,j}$):

$$(1 - \epsilon_{\mathrm{v}}) \epsilon_{sk} V \frac{C^{k,*}_{i,j} - C^{k-1,*}_{i-1,j}}{\Delta t} = \frac{M_{\mathrm{s}}}{\rho_{\mathrm{p}}} \left(C^{*,k-1}_{i+1,j} - C^{*,k-1}_{i,j} \right) - \frac{M_{\mathrm{s}}}{\rho_{\mathrm{p}}} \left(C^{*,k-1}_{i,j} - C^{*,k-1}_{i-1,j} \right)$$

$$+ k'_{\mathrm{m,j}} \left(C^{k-1}_{i,j} - C^{*,k-1}_{i,j} \right) + y^{k-1}_{i,j} \tilde{Q}_{\mathrm{rxn},i} + r^{k-1}_{i,j} \tag{26}$$

and when the desorption rate is greater:

$$(1 - \epsilon_{\mathrm{v}}) \epsilon_{sk} V \frac{C^{k,*}_{i,j} - C^{k-1,*}_{i-1,j}}{\Delta t} = \frac{M_{\mathrm{s}}}{\rho_{\mathrm{p}}} \left(C^{*,k-1}_{i+1,j} - C^{*,k-1}_{i,j} \right) - \frac{M_{\mathrm{s}}}{\rho_{\mathrm{p}}} \left(C^{*,k-1}_{i,j} - C^{*,k-1}_{i-1,j} \right)$$

$$+ k'_{\mathrm{m,j}} \left(C^{k-1}_{i,j} - C^{*,k-1}_{i,j} \right) - y^{*,k-1}_{i,j} \tilde{Q}_{\mathrm{rxn},i} + r^{k-1}_{i,j} \tag{27}$$

2.5.3. Adsorbed species mole balance

The adsorbed species mole balance resembles the pore volume balance and includes the convective term related to solids motion (M_s) but excludes the gas convection terms (Q_rxn). The differential form of the adsorbed species mole balance is:

$$\frac{\partial C^\mathrm{ads}}{\partial t} = \mathcal{D}_\mathrm{S}\frac{\partial^2 C^\mathrm{ads}}{\partial z^2} + V_\mathrm{pore}\left[k_\mathrm{ads}C^*(C_\mathrm{T} - C^\mathrm{ads}) - k_\mathrm{des}C^\mathrm{ads}\right] \tag{28}$$

And, with the finite volume approach is:

$$W_i\frac{C_{i,j}^{ads,k} - C_{i-1,j}^{ads,k-1}}{\Delta t} = -M_\mathrm{s}\left(2C_{i,j}^{ads,k-1} - C_{i,j}^{ads,k-1} - C_{i+1,j}^{ads,k-1}\right) - r_{i,j}^{k-1} \tag{29}$$

3. RESULTS AND DISCUSSION

3.1. Porosity and Geldart group A, B powders

We analyzed the RTD with a pulse input of a mix of tracers including CO_2, CO, H_2, and CH_4 with FCC (Figure 4–a). Diffusivity coefficients for each gas at 25 °C are 0.150 , 0.195 , 0.796 and 0.208 $\mathrm{cm^2\,s^{-1}}$, respectively. Based on previous studies, at high velocity in an empty tube, an extended tail is present. To avoid this physical effect, we operated the reactor at $U_\mathrm{g} = 10\,\mathrm{mm\,s^{-1}}$. The surface area of the FCC—a Geldart group A powder—is $93\,\mathrm{m^2\,g^{-1}}$. All the gases were superimposed in the empty tube studies, except for H_2. The residence time varied with diffusivity with FCC loaded to the reactor (Figure 4–a): At $t =$ 28 s, hydrogen is first detected, and the axial dispersion model fits the data perfectly ($R^2 = 0.990$); 15 s later the MS begins to detect CO and CH_4 (both have similar diffusivity coefficients). When the trailing edge drops to 80 % of the peak height, the curve deviates from an ideal plug flow and the concentration drops more slowly, which corresponds to a large tail. Finally, another 12 s

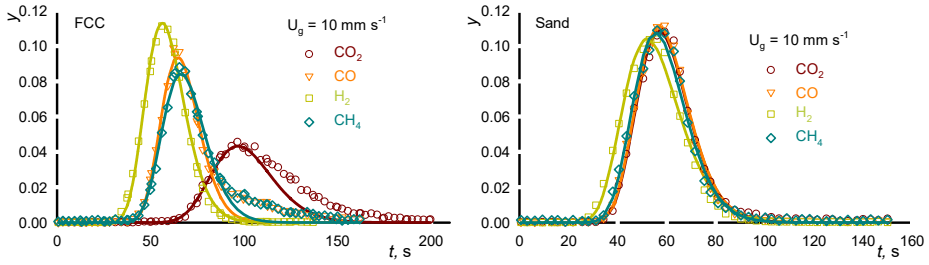

(a) (b)

Figure 4: RTD comparison between Geldart group A and B catalyst: time vs mole fraction, y. The tube was loaded with (a) 8.19 g of FCC – Geldart group A - and (b) 13.5 g of sand – Geldart group B. For FCC (a), the model fits up to the leading edge of the plot, but not the tail where a deviation is observed for CO_2, CO and CH_4. For sand (b), the axial dispersion model fits perfectly the data for all tracers.

later, CO_2 appears—the peak height is much smaller and the tail much more pronounced.

The time it takes for the tracer to reach the MS after the valve switch is the same for both the step-input and pulse. But the axial dispersion model fits the step-input pulse data very well compared to the pulse, which demonstrates that its applicability to identify anomalies and flow heterogeneities is poor (Figure 5).

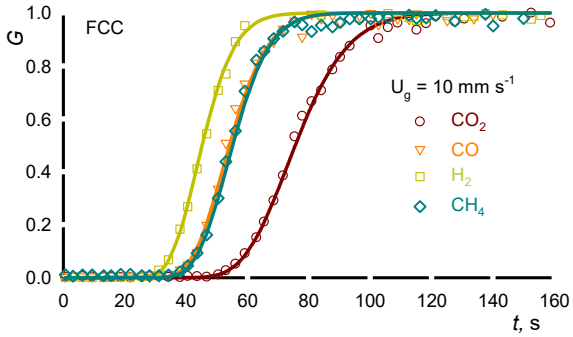

Figure 5: RTD for a step injection at 10 mm s^{-1} with 8.19 g FCC. Argon was initially injected. At $t = 0$, we switched the 4-way valve to substitute the Ar with feed gas—CO_2, CO, H_2, CH_4. The dots represent experimental data while the continuous lines are the fitting axial dispersion model. The tail is impossible to detect with a step injection as opposed to the pulse injection.

We repeated a series of tests with sand—Geldart group B, which has little to no porosity and an order of magnitude lower surface area—$2\,m^2\,g^{-1}$ versus $93\,m^2\,g^{-1}$ (Figure 4–b). The RTD curves for CO, CO_2 and CH_4 resemble that of the empty tube—all three curves are superimposed and the axial dispersion model fits the experimental data very well. Hydrogen egressed the reactor first due to his high diffusivity coefficient, which is again consistent with the previous study about empty tube experiments. Analysis of mean residence time ($\bar{t}$) and variance (σ^2) for FCC and sand powders is present in supplementary file.

We attribute the difference between FCC and sand RTD to several factors:

1. **Diffusion**: hydrogen has a diffusivity coefficient four to five times higher than CO, CO_2 and CH_4 ($0.796\,vs\,0.150\,to\,0.208\,cm^2\,s^{-1}$). Thus, for RTD experiment with FCC and sand, H_2 exit the reactor 10 to 15 s before CO at $10\,mm\,s^{-1}$. Radial diffusion of hydrogen ensures a flat concentration profile so that axial dispersion model fits the experimental data well.
2. **Porosity**: The physico-chemical properties of the gas tracer affect the RTD for porous powders more than for non-porous and the effect increases with longer residence time.
3. **Adsorption**: Diffusivity is insufficient to account for the extended CO_2 tail for the case with FCC: The RTD curve is delayed by 12 seconds after CO and CH_4. We attribute this phenomena to a chromatographic effect where CO_2 ingress into the pores and then interacts/adsorbs to the internal surface. As the tracer passes and the concentration decreases, the driving force reverses and the CO_2 desorbs. This process is on the order of the mixing time of the solids in the bed, which could then extend the residence time (CO_2 adsorbing at the top of the bed is carried down with the solids as the recirculate to the bottom of the reactor [29]).

3.2. New model results

For each syngas tracer, we applied the new model (Figure 6). We omitted H_2 and resolved simultaneously three mole balances for CO_2, CO, and CH_4. Hydrogen has a high diffusivity coefficient and other phenomena that are unaccounted for with the new model.

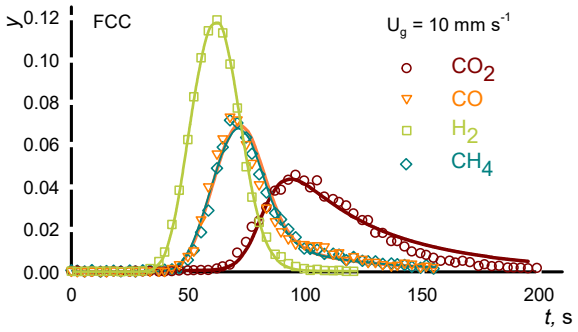

Figure 6: New model fitting results for FCC. Same conditions as Figure 4. The model predicts dispersion, diffusion, and adsorption phenomena.

First, we calculated the molar concentration at each MS time step and normalized the data to have identical area under the curve for all tracers. The gas concentration detected at the bottom of the reactor (including the entrance lines and the MS capillary) is applied as the initial concentration in the model simulation. To fit the model, we minimized the sum of squares error (SSE) between the data and the new model for all the tracers together (CO_2, CO and CH_4). The parameters adjusted (Table 3) are the volumetric flow rate (Q), the circulation flow (M_s), the mass transfer between the bulk phase and pores ($k'_{m_{CO_2}}$, $k'_{m_{CO}}$, $k'_{m_{CH_4}}$, $k'_{m_{H2}}$), the adsorption rate ($k_{ads_{CO2}}$, $k_{ads_{CO}}$, $k_{ads_{CH4}}$) and desorption ($k_{des_{CO2}}$, $k_{des_{CO}}$, $k_{des_{CH4}}$). When we reached the highest R^2 for the first three tracers, we fit the hydrogen data by minimizing SSE with the flow rate. We maintained CO_2, CO, and CH_4 parameters. For all tracers, we fitted the first 200 s with an optimal number of CSTR of 40.

Tracer	Q ($\mathrm{mL\,min^{-1}}$)	k'_{m} ($\mathrm{m^3\,s^{-1}}$)	k_{ads} ($\mathrm{mol^{-1}\,s^{-1}}$)	k_{des} ($\mathrm{mol^{-1}\,s^{-1}}$)	V_{T} ($\mathrm{kmol\,kg^{-1}}$)	R^2
CO_2		4.8×10^{-7}	31700	124		0.986
CO	19.3	2.0×10^{-5}	4.92	0.0703	3.19×10^{-6}	0.970
CH_4		2.1×10^{-5}	4.92	0.0703		0.986
H_2	22.5	3.2×10^{-6}	0	0	0	0.999

Table 3: New model parameters adjusted for a pulse injection RTD in a quartz tube loaded with 8.19 g FCC - velocity of $10\,\mathrm{mm\,s^{-1}}$. M_{s} is 9.59×10^{-5} for each gases.

The new model predicts the adsorption of CO_2 compared to the axial dispersion model. Indeed, the coefficient of determination (R^2) has a higher value for CO_2 (0.920 vs 0.986), CO (0.946 vs 0.970), CH_4 (0.979 vs 0.986), and H_2 (0.990 vs 0.999). However, the R^2 for CO and CH_4 with the new model is due to the difference in height and a slight shift to the right (Figure 6) while for the axial dispersion model the low R^2 value is due by the deviation in the descending tail (Figure 4—a). Section 3 of the supplementary file present the comparison between the results with the axial dispersion model and the new model.

The new model is flexible and adjusts from simple cases, plug flow behaviour, to a complex situation with adsorption. The H_2 molecules, with its small size and its high diffusivity coefficient, exit the reactor first. To compensate for this effect, we increased the flow rate from $19.3\,\mathrm{mL\,min^{-1}}$ to $22.5\,\mathrm{mL\,min^{-1}}$. To simplify the model, we assumed that carbon monoxide and methane have the same adsorption and desorption rate. Then, only the mass transfer between the bulk phase and the pores is different. Finally, the new model confirms the hypothesis where CO_2 is adsorbed by FCC catalyst and quantify the phenomena. The desorption rate is 256 times faster than the adsorption rate. The concentration of the vacant site (V_{T}) equals $3190\,\mathrm{nmol\,g^{-1}}$. The tail is well represented with this model ($R^2 = 0.986$).

3.3. New model—Sensitivity analysis

To analyze the sensitivity of the new model, we varied one parameter at the time while all other variables are at their optimum values. Then we compared the R^2. We analyzed the effect of the number of CSTRs, the time modeling, and the volumetric flow rate. The last one is minimized when we resolved the mole balance equations while n_{CSTR} and time are a chosen value.

3.3.1. Number of CSTRs

We analyzed the effect of the number of CSTRs on the R^2 with three syngas species (Figure 7—a) and then consider the hydrogen data independently The R^2 increases reaches a plateau around $n_{\mathrm{CSTR}} = 30$ for the three species. At this point, the R^2 of the hydrogen decreases slightly. When we increase n_{CSTR} from 30 to 45 (Figure 7—b), the R^2 of CH_4 continues to increase but it reaches a plateau for CO and CO_2. The maximum R^2 for CO_2 is 0.9863 and finally selected 40 CSTRs as the optimum value for parameter estimation.

When we increase the number of CSTR, the RTD curves for CO_2 are higher and slide to the right (Figure 7—c). At 40 CSTRs, the height of the fitting curve is the same as the data. At 45 CSTRs, the model deviates from the data at the trailing edge, thus the R^2 is lower. The tails are similar to each curve which confirms that the n_{CSTR} is independent of the slope shape.

3.3.2. Volumetric flow rate

The volumetric flow rate is a measured variable but due to the uncertainty in its value, we take it as a parameter since a small deviation greatly influences the R^2. For example, for CO_2, a variation of 9 % in the flow rate can decrease the R^2 of 83 %. The model is unstable for $Q < 16.455\,\mathrm{mL\,min^{-1}}$ (which depends on the time step). We fit the data from 16 5 to $30\,\mathrm{mL\,min^{-1}}$— the injection volumetric flow rate. In general, the R^2 increases up to a maximum and decreases

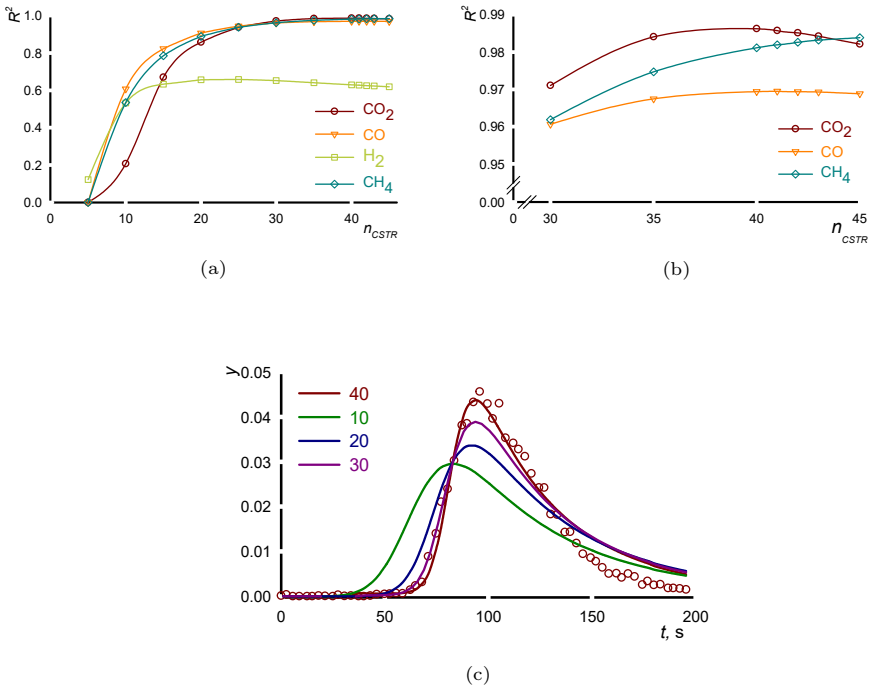

Figure 7: Sensitivity analysis on the number of CSTRs. (a) R^2 vs the number of CSTR for the four tracers. (b) Variation of R^2 for CO_2, CO, and CH_4 for $n_{\mathrm{CSTR}} = 30$ to 45. (c) RTD curves for CO_2 adsorption on FCC catalyst. The dots are the CO_2 data while the lines are the new model fits with n_{CSTR} from 10 to 40. The optimal value is $n_{\mathrm{CSTR}} = 40$.

immediately – bell shape (Figure 8—a). We expanded the range of the axes to better differentiate between the three species (19—20 mL min^{-1}) – R^2 variation is 5 % (Figure 8 —b). At this flow rate zone, the CH_4 decreases while the CO increases. The optimum, where CO crosses CH_4, is 19.5 mL min^{-1}. However, CO_2 reached a maximum at 19.3 mL min^{-1} and then decreased. This is in accordance with the value obtained by minimizing the SSE – 19.3 mL min^{-1}.

We plot the RTD curve for CO_2 with the new model and flow rate from 18 to 20 mL min^{-1} (Figure 8— c). At 18 mL min^{-1}, the solver becomes unstable with the presence of random peaks. The R^2 decreasing by 10 % with a change of 2 % in the flow rate. With an increase in flow, the curve is shifted to the left and becomes taller. However, the adsorption tail is independent of the flow

rate.

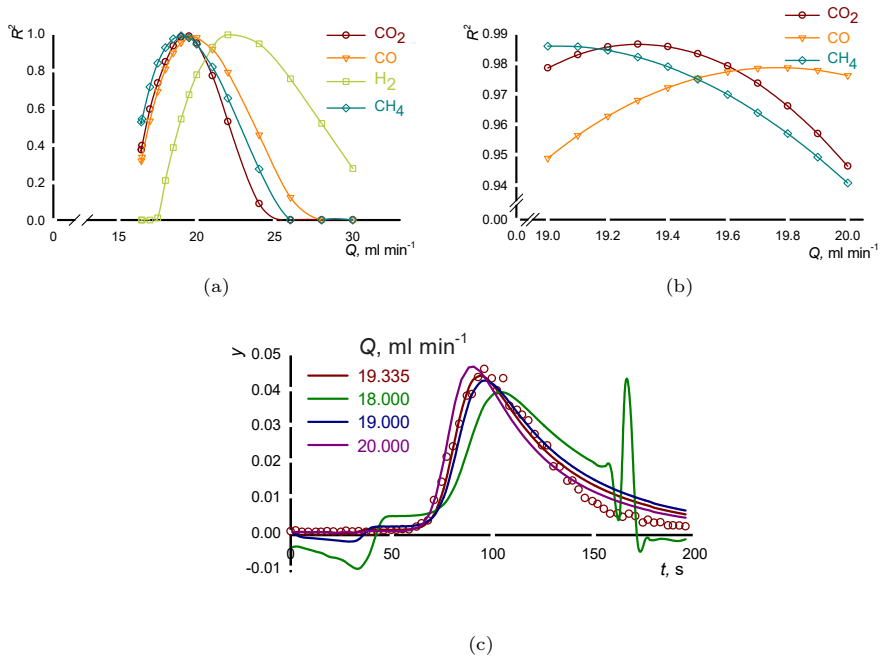

Figure 8: Sensitivity analysis of the volumetric flow rate. (a) R^2 vs the flow rate for four tracers. (b) Variation of R^2 for CO_2, CO, and CH_4 for $Q = 19$ to 20 mL min^{-1}. (c) RTD curves for CO_2 adsorption on FCC catalyst. The flow rate varies from 18 to 20 mL min^{-1}. The optimal value is $Q = 19.3$ mL min^{-1}.

3.3.3. Modeling time

The total time from the injection of the tracers until the entire 10 mL pulse exits the reactor is approximately 100 s for H_2, 150 s for CO and CH_4, and 200 s for CO_2. We started the analysis at 110 s due to the instability to resolve under this time (Figure 9—a). The R^2 for hydrogen is lower from 120 to 200 s compared to 110 s. This is a common observation when we include time in the modeling beyond which the concentration reaches a steady value [1]. The R^2 is stabilized at 140 s for CO_2, CO and CH_4 (Figure 9—b). Indeed, the maximum variation in R^2 for each 10 s is 0.07 % for CO, 0.09 % for CH_4, and 0.11 % for CO_2. Thus, we concluded that from 140 s of modeling time, the model fits the

data except for H_2 where its optimum point is at 110 s. It is confirmed with the RTD curve for CO_2 with different time modeling (Figure 9—c). At 110 s, the model fit is slightly shifted to the left and the peak is higher.

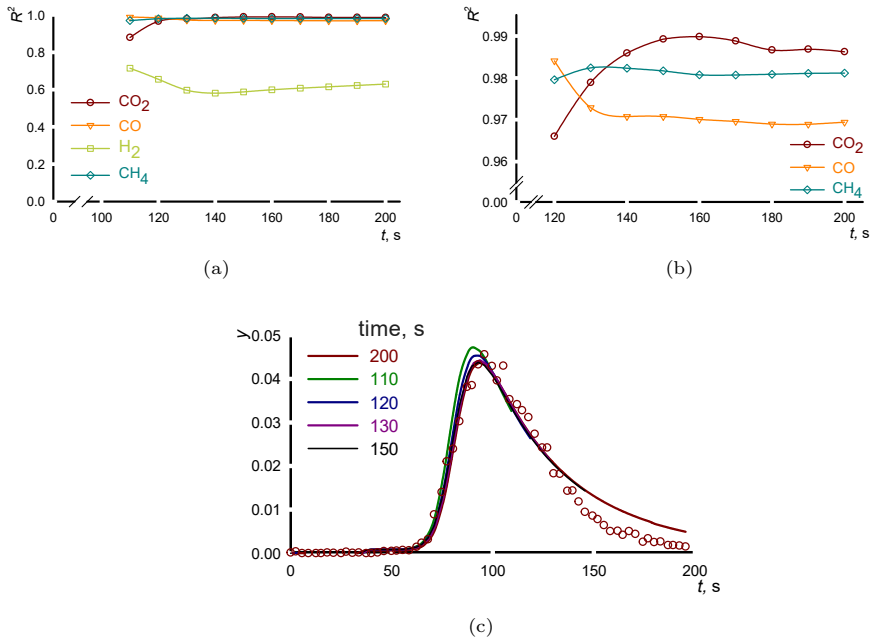

Figure 9: Sensitivity analysis of modeling time. (a) R^2 vs the modeling time for the four tracers (b) Variation of R^2 for CO_2, CO, and CH_4 for time = 120 to 200 s. (c) RTD curves for CO_2 adsorption on FCC catalyst. The modeling time is from 110 to 150 s. At 150 s or higher, the fitting results are the same.

3.4. Temperature analysis

To confirm the impact of diffusivity on RTD, we compared empty tube, FCC and sand with a pulse injection at 300 °C (Figure 10). The syngas tracers—CO_2, CO, CH_4, and H_2—are fed at 10 mm s^{-1}. At this temperature, diffusivity coefficients are 0.479 , 0.622 , 0.664 , and 2.54 cm^2 s^{-1} respectively. The first hypothesis was:

- The larger the difference of diffusivity coefficient is between the gases, the larger will be the delay between each RTD curve.

At 25 °C and 300 °C, the hydrogen diffusivity coefficient is 5 times that of CO_2 and 4 times that of CO and CH_4. According to this hypothesis, the MS should detect H_2 much sooner than the others. However, only hydrogen is slightly advanced compared to CO_2, CO and CH_4, which overlap. Thus, if the ratio (Ex. $H_2/CO = 4$) is kept, the delay between RTD curve will be the same. Curiously, at 300 °C the CO_2 egresses at the same time at the other gases with FCC indicating that adsorption is absent (Figure 10–b). Thus we conclude:

1. The experimental technique is capable of identifying the contribution of diffusivity to the RTD when the diffusion coefficient is at least 2 times greater than any other tracer (the curve of the gas with the highest diffusion coefficient shifts to the left). This observation is valid for porous and non-porous powders (Figure 10–b,c).
2. Even at 300 °C and $14 \times U_{\mathrm{mf}}$, the pulse technique is capable of identifying the effect of diffusion coefficient on the RTD (Supplementary file—Figure S2).
3. Small atomic gases like H_2 and He with high diffusivity coefficient will experimentally fit the axial dispersion model for all velocity and temperatures (Figure 10).

4. CONCLUSION

Residence time distribution is an effective tool to detect bypassing, dead volume, and back mixing. We analyzed gas phase RTD in an 8 mm internal diameter, 36 cm long quartz tube fluidized bed. We injected simultaneously, at $10\,\mathrm{mm\,s^{-1}}$, a syngas mix of gases—CO_2, CO, CH_4 and H_2 and characterized the data with the axial dispersion model. When the reactor is loaded with FCC—a porous catalyst, hydrogen, with its high diffusivity coefficient, egressed the reactor 15 s before CH_4/CO and 27 s before CO_2. Also, an extended tail is

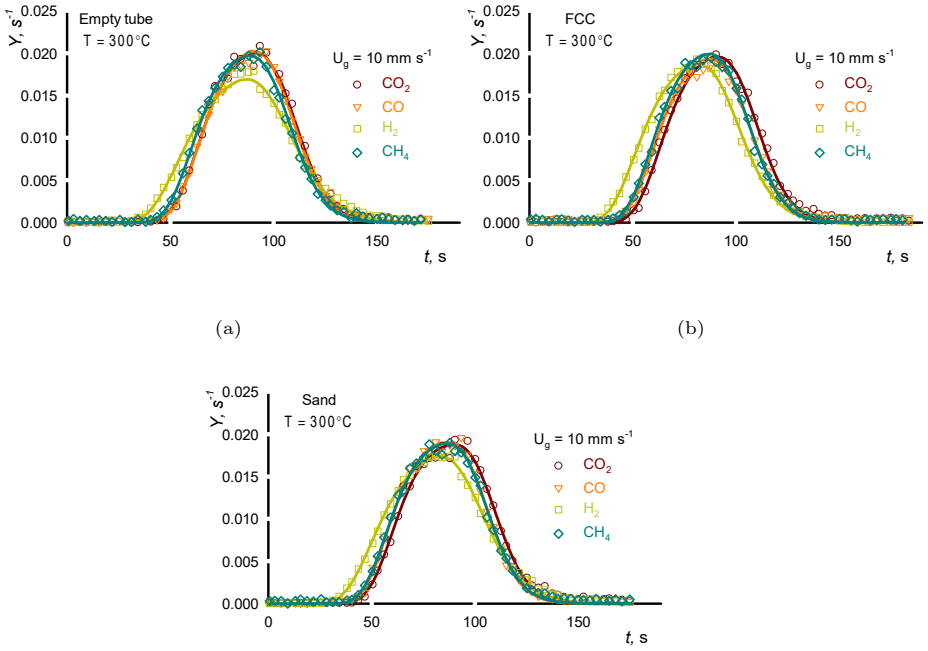

Figure 10: Residence time distribution comparison at 300 °C: time vs $Y = \frac{C_i}{\sum C_i \Delta t}$. The quartz tube was (a) empty or loaded with (b) 6.50 g of FCC and (c) 10.7 g of sand. The tapped bed height was 13 cm.

observable for CO_2, CO, and CH_4 (more pronounced for CO_2). The axial dispersion model deviates from the experimental data because the model assumes ideal behaviour (R^2 $CO_2 = 0.920$). We compared the results with a non-porous catalyst—sand. All the RTD curves overlap, except for hydrogen.

We developed a *tanks-in-series* model considering three phase: the gas phase, gas in catalyst pores, and the adsorbed species. We quantify the mass transfer between the bulk phase and the pores (k_m), the circulation rate (M_s), and the real volumetric flow rate (Q). The adsorption rate (k_ads) and desorption rate (k_des) for CO_2 is 31 719 s^{-1} and 123.8 s^{-1} respectively with a concentration of vacant sites of 3.1886×10^{-6} kmol kg^{-1}. For CO and CH_4 k_ads and k_des are lower i.e. 4.9201 s^{-1} and 0.070 349 s^{-1}. We increased the R^2 from 0.920 with

the axial dispersion model to 0.986 with the new model.

To resolve the entire system, we, first, omitted hydrogen due to its 4 to 5 times higher diffusivity coefficient ($\mathscr{D} = 0.796\,\mathrm{cm^2\,s^{-1}}$). We choose 40 CSTRs in series – the optimum value. Then, we minimized the sum of square errors (SSE) on all parameters for CO_2, CO, and CH_4 simultaneously. The total volumetric flow rate (Q) is interdependent of each adsorbed species. Indeed, when a species is adsorbed, Q decreases. Inversely, when a species is desorbed, Q increases.

The new model quantity the adsorption phenomena but has a few limitations. First, the number of CSTRs is fixed at 40 for all the species. However, CO_2 is far from ideal so should have less CSTRs while H_2, with little dispersion, should have several hundred CSTRs. The fact that the model is resolved simultaneously with all the tracers limits required that we better account for the effect of H_2 diffusivity. However, for all practical situations operating at high temperature, differences in diffusivity are unimportant. This highlights the importance of carefully choosing tracers for cold flow studies but at temperatures of 300 °C the physico-chemical properties of the gas tracer species is less critical.

Then, we must set initial values in the Fortran program for all parameters (Table 4). If these values are out of the range, the solver will diverge. A substantial amount of time is required to find this data interval.

Another simplification made to decrease the computational time is to fix the adsorption and desorption rate for CO and CH_4 at the same values ($k_{\mathrm{ads,CO}} = k_{\mathrm{ads,CH4}}$) and ($k_{\mathrm{des,CO}} = k_{\mathrm{des,CH4}}$). This assumption is valid considering extended tail for the 2 species are almost indistinguishable. However, to improve the model, distinct values will account for more of the variance in the experimental data.

Parameter	Range
n_{CSTR}	5 to 45
Volumetric flow rate (Q)	16.455 to 30 mL min^{-1}
Circulation rate (M_{s})	0.0001 to 0.001 kg s^{-1}
$k_{\mathrm{m_{CO_2}}}$ $k_{\mathrm{m_{CH_4}}}$ et $k_{\mathrm{m_{CO}}}$ $k_{\mathrm{m_{H_2}}}$	8×10^{-9} to 1×10^{-6} 0 to 2.2×10^{-5} 0 to 2×10^{-5}
$k_{\mathrm{ads_{CO_2}}}$ $k_{\mathrm{ads_{CO}}} = k_{\mathrm{ads_{CH4}}}$	18600 to 35050 3×10^{-4} to 44
$k_{\mathrm{des_{CO_2}}}$ $k_{\mathrm{des_{C}O}} = k_{\mathrm{des_{CH_4}}}$	27 to 144 8×10^{-6} to 1.1
Vacant site (V_{T})	2.88×10^{-6} to 3.24×10^{-6} kmol kg^{-1}
Modelling time	110 to 200 s

Table 4: New model limits range for an 8 mm fluidized bed reactor. The leftover parameters are fixed at their optimum values. Outside this range, the solver diverge.

NOMENCLATURE

C—concentration, mol L^{-1}

C_{A}—concentration of A in the gas, mol L^{-1}

C_{A}^{i}—concentration of A at the gas-particle interface, mol L^{-1}

$C_{\mathrm{A,b}}$—concentration of A in the bubble phase, mol L^{-1}

C^{*}— concentration gas phase inside a pore, mol L^{-1}

C^{ads}—concentration adsorbed species, mol L^{-1}

$\mathscr{D}$—diffusivity coefficient, cm^2 s^{-1}

$\mathcal{D}$—axial dispersion coefficient, m^2 s^{-1}

$\mathcal{D}_{\mathrm{S}}$—axial dispersion coefficient for solid phase, m^2 s^{-1}

d_{p}—particle diameter, m

d_{pore} —pore diameter, m

f_{i}—prediction data

g—gravity, m s^{-2}

H_r —Hausner ratio, dimensionless

K_GB—interchange coefficient between bubble and emulsion-cloud, s^{-1}

k_ads—adsorption coefficient, $\mathrm{mol}^{-1}\,\mathrm{s}^{-1}$

k_des—desorption coefficient, $\mathrm{mol}^{-1}\,\mathrm{s}^{-1}$

k_gc—mass transfer coefficient between bubble-cloud and emulsion, $\mathrm{m\,s}^{-1}$

k'_m—mass transfert coefficient, $\mathrm{m}^3\,\mathrm{s}^{-1}$

M_m—axial mixing coefficient, $\mathrm{m}^2\,\mathrm{s}^{-1}$

M_s—solids circulation flow term (convection), $\mathrm{kg\,s}^{-1}$

N_A—mol of A, mol

N_Pe—Peclet number, dimensionless, $[uZ/\mathcal{D}]$

N_Re—Reynolds number, dimensionless

n_CSTR—number of CSTRs in series

P—pressure, Pa

P_o—atmospheric pressure, Pa

Q_rxn—volumetric flow rate / convective term, $\mathrm{mL\,min}^{-1}$

$\tilde{Q}_\mathrm{rxn}$—molar flow rate, $\mathrm{mol\,s}^{-1}$

R—gas constant, $[8.314\,\mathrm{J\,mol}^{-1}\,\mathrm{K}^{-1}]$

R^2—coefficient of determination, dimensionless

r—reaction rate, $\mathrm{mol\,L}^{-1}\,\mathrm{s}^{-1}$

S_A —specific surface area, $\mathrm{m}^2\,\mathrm{g}^{-1}$

$S_\mathrm{ex,cloud}$—exterior surface of clouds m^2

T—temperature, °C

t—time, s

$\bar{t}$—mean residence time, s

U_g—gas velocity, $\mathrm{m\,s}^{-1}$

U_mf—minimum fluidization velocity, $\mathrm{m\,s}^{-1}$

u_b—bubble rise velocity, $\mathrm{m\,s}^{-1}$

V—total volume of the system, m^3

V_{bubble}—volume occupied by the bubble phase, m^3

V_{cloud}— volume occupied by cloud and bubble, m^3

V_{g} - volume of the gas phase, m^3

V_{p} - volume of the gas in the particle phase, m^3

V_{T} - number of vacant sites

v_{pore}—specific pore volume, $\mathrm{mL\,g^{-1}}$

W—mass of catalyst, g

w—flux, $\mathrm{kg\,m^{-2}\,s^{-1}}$

w_{s}—mass flux, $\mathrm{kg\,s^{-1}\,m^{-2}}$

X_{A}—cross sectional area, m^2

y—fraction, dimensionless

$\bar{y}$—mean of experimental data

y_{i}—experimental data

Z—characteristic system length, m

z—length, m

Greek Letters

ΔP—pressure drop, Pa

ΔZ—bed height, m

ϵ_{v}—void fraction, dimensionless

ϵ_{sk}—skeletal void fraction, dimensionless

μ - viscosity, $\mathrm{kg\,m^{-1}\,s^{-1}}$

ϕ—sphericity, dimensionless

ρ_{b}—bulk density, $\mathrm{kg\,m^{-3}}$

ρ_{g}—gas density, $\mathrm{kg\,m^{-3}}$

ρ_{p}—particle density, $\mathrm{kg\,m^{-3}}$

ρ_{sk}—skeletal density, $\mathrm{kg\,m^{-3}}$

σ^2—variance, s^2

θ—dimensionless time, $[tu/Z]$

θ_{ang}—angle of repose, $^\circ$

ξ—dimensionless distance, $[z/Z]$

Indice

c—cloud phase

e—emulsion phase

i—grid

j—species

k —time

p—phase (emulsion (E), bubble (B), and solid (S))

5. Acknowledgment

This research was undertaken, in part, thanks to funding from the Canada Research Chairs program and the authors gratefully acknowledge the financial support from the Natural Sciences and Engineering Research Council of Canada (NSERC) and the Canada Foundation for Innovation (CFI).

References

[1] A. Bérard, B. Blais, G. S. Patience, *The Can. J. Chem. Eng.* **2020**, *98*, 848.

[2] M. Escotet-Espinoza, S. Moghtadernejad, S. Oka, Y. Wang, A. Roman-Ospino, E. Schäfer, P. Cappuyns, I. V. Assche, M. Futran, M. Ierapetritou, F. Muzzio, *Powder Technol.* **2019**, *342*, 744.

[3] M. Stec, P. M. Synowiec, *Can. J. Chem. Eng.* **2017**, *95*, 2410.

[4] P. Wojewodka, R. Aranowski, C. Jungnickel, *J. Ind. Eng. Chem.* **2019**, *69*, 370.

[5] C. W. Chan, J. P. Seville, D. J. Parker, J. Baeyens, *Powder Technol.* **2010**, *203*, 187.

[6] R. Andreux, G. Petit, M. Hemati, O. Simonin, *Chem. Eng. Process. Process. Intensif.* **2008**, *47*, 463.

[7] J. Zhang, G. Xu, *Particuology* **2015**, *19*, 155.

[8] M. Dulle, H. Ozcoban, C. Leopold, *Int. J. Pharm.* **2019**, *555*, 220.

[9] Z. Zou, Y. Zhao, H. Zhao, L. Zhang, Z. Xie, H. Li, Q. Zhu, *Chin. J. Chem. Eng.* **2017**, *25*, 1706.

[10] L. Hua, J. Wang, J. Li, *Chem. Eng. Sci.* **2014**, *117*, 264.

[11] T. Li, Y. Zhang, J. R. Grace, X. Bi, *AIChE J.* **2010**, *56*, 2280.

[12] S. Geng, Z. Han, J. Yue, Y. Li, X. Zeng, D. Lai, J. Yu, G. Xu, *Chem. Eng. J.* **2018**, *351*, 110.

[13] W.-C. Yang, W.-C. Yang, ed., Handbook of fluidization and fluid-particle systems, chapter 3, Marcel Dekker, New York **2003**, pp. 63–121.

[14] J. Zhang, A. R. Teixeira, L. T. Kögl, L. Yang, K. F. Jensen, *AIChE J.* **2017**, *63*, 4694.
URL `https://aiche.onlinelibrary.wiley.com/doi/abs/10.1002/aic.15807`

[15] K. A. Hweij, F. Azizi, *Chem. Eng. J.* **2015**, *279*, 948.

[16] G. Patience, Circulating Fluidized Beds: Hydrodynamics and Reactor Modelling, Thesis **1990**.

[17] A. Drinkenburg, K. Rietema, *Chem. Eng. Sci.* **1972**, *27*, 1765 .

[18] W. Yang, Handbook of Fluidization and Fluid-Particle Systems, Marcel Dekker, Inc., Pittsburgh, Pennsylvania, U.S.A. **2003**.

[19] D. Kunii, O. Levenspiel, D. Kunii, O. Levenspiel, eds., Fluidization Engineering (Second Edition), second edition edition, Butterworth-Heinemann, Boston **1991**, pp. 1 – 491.

[20] B. Partridge, R. P.N., *Trans. Inst. Chem. Engrs.* **1966**, *44*, 335.

[21] D. Wippern, K. Wittman, J. Kuhne, H. Helmrich, K. Schügerl, *Chem. Eng. Commun.* **1981**, *10*, 307.

[22] D. Geldart, *Powder Technol.* **1973**, *7*, 285.

[23] M. Menéndez, J. Herguido, A. Bérard, G. S. Patience, *The Can. J. Chem. Eng.* **2019**, *97*, 2383.

[24] L. Vinnett, F. Contreras, A. Lazo, M. Morales, F. Díaz, K. Waters, *Miner. Eng.* **2018**, *115*, 41.

[25] N. Vargaftik, Handbook of physical properties of liquids and gases, 2nd edition, Springer-Verlag Berlin Heidelberg **1975**.

[26] P. Perreault, E. Robert, G. S. Patience, *The Can. J. Chem. Eng.* **2019**, *97*, 1036.

[27] L. Lapidus, N. R. Amundson, *J. Phys. Chem.* **1952**, *56*, 984.

[28] G. S. Patience, Y. Farrie, J.-F. Devaux, J.-L. Dubois, *Chem. Eng. & Technol.* **2012**, *35*, 1699.

[29] J. Yates, J. Constants, *Chem. Eng. Sci.* **1973**, *28*, 1341 .